ELSEVIER

Nuclear Instruments and Methods in Physics Research A 427 (1999) 528–542

NUCLEAR INSTRUMENTS & METHODS IN PHYSICS RESEARCH Section A

A warm-liquid calorimeter for cosmic-ray hadrons

J. Engler*, F. Fessler, J.R. Hörandel, T. Holst, H. Keim, H.J. Mathes, H.H. Mielke[1], J. Milke, U. Raidt[2], J. Wochele

Institut für Kernphysik, Forschungszentrum und Universität Karlsruhe, P.O. Box 3640, D-76021 Karlsruhe, Germany

Received 10 August 1998; received in revised form 5 January 1999

Abstract

An iron sampling calorimeter for cosmic-ray hadrons used in the centre of a large air shower experiment is described. The iron absorber is interspersed with eight layers of ionisation chambers filled with the room-temperature liquids tetramethylsilane and tetramethylpentane. Experiences gained from the calorimeter, its performance and long-term stability are presented. For energies in the TeV range shower profiles and transition curves have been measured and are compared with Monte Carlo calculations employing the FLUKA code. Good agreement has been found except in the lateral halo region. In the outer regions the energy deposition found is smaller than that obtained by the simulations.

PACS: 29.40.Cs; 29.40.Vj; 96.40.Pq

Keywords: Hadron sampling calorimeter; Liquid ionisation chambers; Cosmic-ray hadrons; TMS calorimeter; TMP calorimeter; Hadronic shower simulation

1. Introduction

In cosmic-ray physics, when measurements have to be carried out above the atmosphere, special devices for calorimetric detection of hadrons have been used. Due to weight and size limitations, mostly "single-layer calorimeters" were applied. They detect hadrons by conversion in a relatively thin layer of about one interaction length in thickness. At the highest energies in the PeV region and above, however, the flux of primary particles becomes so small that the necessarily large area installations can be realized on the earth's surface only.

Within the framework of the Karlsruhe extensive air shower experiment KASCADE [1,2], the central core of showers is investigated using a totally absorbing sampling calorimeter. The aim of the KASCADE experiment is to determine the mass composition of primary cosmic rays in the energy domain of 10^{14}–10^{17} eV and to measure reliably the cosmic-ray energy spectrum. The hadron content of an air shower at sea level decisively depends

* Corresponding author. Fax: + 49-7247-82-4047.
E-mail address: engler@ik1.fzk.de (J. Engler)
[1] Now at: Hewlett–Packard GmbH, Herrenbergerstrasse 135, D-71004 Böblingen, Germany
[2] Now at: Alcatel SEL AG, Lorentzstrasse 10, D-70435 Stuttgart, Germany.

0168-9002/99/$ - see front matter
PII: S0168-9002(99)00051-0

on the mass of the primary particle. Roughly speaking, iron nuclei initiate cascades with fewer hadrons and less hadronic energy at ground level than primary protons of the same total energy. Cascades initiated by high-energy photons should contain almost no hadronic energy at all. A hadron calorimeter, therefore, is well suited to distinguish air showers initiated by different primaries.

Such a calorimeter should be able to detect hadrons up to 10 TeV and more. For a good energy resolution it should be deeper than 10 nuclear interaction lengths λ_I. In order to distinguish individual hadrons within the core and to determine their energies separately, a relatively fine lateral segmentation is desirable. For instance, it is of interest to know the energy of the most energetic hadron, since it is a parameter closely related to the primary's mass. A major challenge of cosmic rays at the highest energies is their small particle flux requiring large detector surfaces. To accumulate 100 particles per annum at 10 PeV, a calorimeter surface of 300 m^2 is needed. This is the size of the KASCADE calorimeter.

The active elements of the calorimeter consist of liquid ionisation chambers containing the liquids tetramethylsilane (TMS) and tetramethylpentane (TMP) as dielectric. The calorimeter is the first large scale device being operated using this technique. A prototype of this calorimeter having the identical longitudinal configuration, but 5% of its lateral size only, and the original instrumentation has been operated for nearly three years and the experience and results on transition curves have been published elsewhere [3]. It is the intention of this article to report on the performance of the large calorimeter which is taking data for three years by now, especially on the warm-liquid ionisation chambers.

It is also of interest to find out how well the existing shower simulation codes such as FLUKA [4,5], which is widely used for the design of LHC detectors, describe hadronic cascades in the TeV region. We cannot test the absolute amount of energy deposition due to the lack of calibration possibilities at accelerators, but we can determine the longitudinal and lateral profiles of energy deposition, thereby examining the reliability of the Monte Carlo codes.

2. Calorimeter set-up

A sketch of the central KASCADE calorimeter is shown in Fig. 1. It is constructed from casted Fe

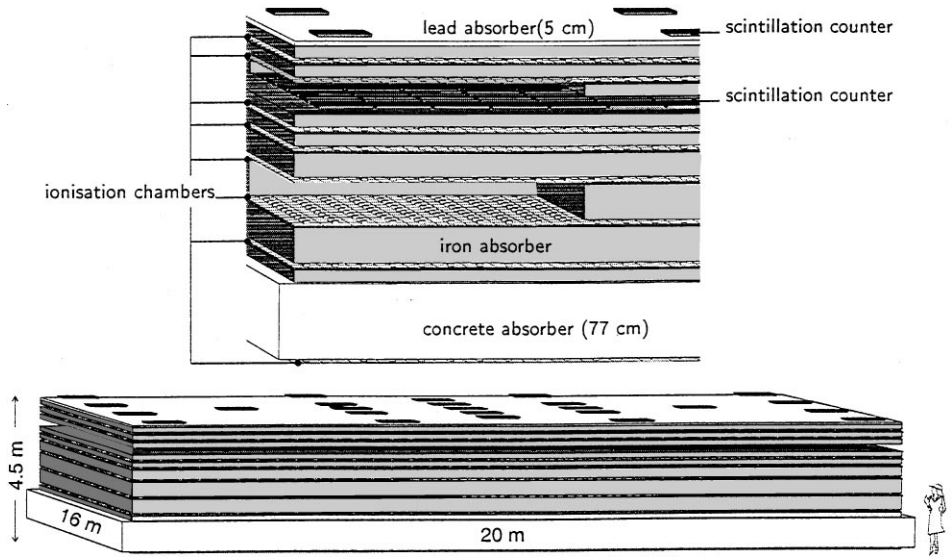

Fig. 1. Schematic view of the KASCADE central calorimeter.

slabs, 12 cm thick, leaving eight slots free to introduce active elements. Seven slots are filled with liquid ionisation chambers, whereas scintillation counters for fast-trigger purposes are inserted into the space behind the third iron layer where hadron showers of 100 GeV reach their maximum of energy deposition. The last layer of ionisation chambers is situated below the concrete ceiling, which acts as a tail catcher of $2.5\lambda_I$ in thickness. The total depth of the calorimeter for vertical protons amounts to 11.5 interaction lengths ensuring a reasonable shower containment up to 25 TeV. At this energy on average 97.5% of the energy is deposited in the calorimeter.

As can be seen from Fig. 1, sampling is constant at the top and becomes coarser, namely 24 and 36 cm, in deeper layers where the mean transition curve drops exponentially. For cosmic-ray hadrons a very good energy resolution is not mandatory at the highest energies. We therefore, deliberately renounce on the $1/\sqrt{E}$ improvement with the rising energy in case of a calorimeter with constant sampling steps. Yet, the usual caveat applies, when dealing with a flux spectrum that is steeply falling with energy. Due to a finite resolution, the energy is systematically reconstructed too high, and the energy resolution is a critical parameter. To keep the correction for this shift small, a reasonably good resolution is desirable. According to MC calculations, the calorimeter resolutions varies slowly from $\sigma(E)/E = 20\%$ at 100 GeV to 10% at 10 TeV. The systematic bias of the reconstructed energy due to the strongly falling energy spectrum has been estimated to amount to 20% in the TeV region. On top of the upper iron absorber, a 5 cm lead layer suppresses the electromagnetic component to a sufficiently low level.

The trigger plane consists of 456 plastic scintillators read out by wavelength shifter bars to obtain a uniform signal response. The scintillators cover two thirds of the surface and deliver a timing information with 1.8 ns resolution [6]. The trigger layer is situated behind a material corresponding to 2.2 interaction lengths, hence, 11% of all hadrons convert in deeper parts of the calorimeter. This position has been chosen as a compromise between a good efficiency at high energies and a threshold as low as possible.

Data were taken with two types of trigger conditions:

(a) at least eight scintillators show a signal above $\frac{1}{3}$ of that from a passing muon (muon trigger),

(b) at least one scintillator has a signal that corresponds to more than 50 passing muons (hadron trigger).

For hadrons above 1 TeV both conditions are fulfilled in more than 90% of all cases.

3. Liquid ionisation chambers

The structure of an ionisation chamber is sketched in Fig. 2. It consists of a $50 \times 50 \times 1\ \text{cm}^3$ stainless-steel box containing four electrodes ($25 \times 25\ \text{cm}^2$) positioned in the mid-plane of the box by ceramic spacers. A ceramic feed-through allows to apply high voltage to the electrodes and to read ut their signals independently, ensuring a fine spatial segmentation of the calorimeter.

Several high-mobility liquids exist, which are suitable for particle detection in calorimeters [7]. These liquids show electron conduction. Free excess electrons, e.g. from an ionisation process, move under the influence of an electric field in a conduction band similar to those of semiconductors. For our purpose, a high signal yield and low costs were the decisive criteria, whereas a fast signal generation, hence, a high drift velocity was of minor importance. TMS has been chosen due to its relatively favourable price, but despite of its lower charge yield hexamethyldisilane (HMDS) would have been an alternative solution due to its low costs [8]. One third of the calorimeter is equipped with TMP which has been taken over from the UA1 upgrade calorimeter at CERN.

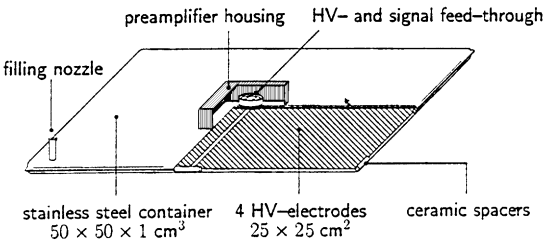

Fig. 2. Sketch of a liquid ionisation chamber.

The costs of a chamber being mainly determined by the price of the liquid, the thickness was chosen as a compromise between affordable costs and a reasonable signal/noise ratio for minimum ionising particles. A ratio of 2:1 was taken to be sufficient to recognize the pattern of a muon passing through the eight active layers of the iron absorber.

An important quantity which determines the operational capability of an ionisation chamber is the lifetime τ of free electrons in the liquid. It should be much greater than the electrons' drift time in order to collect the total charge produced. The lifetime is limited by the presence of electron-attaching impurities or scavengers of concentration $[s]$ and is given by

$$\tau = \frac{1}{k\,[s]}$$

where k is the rate constant for the attachment process. Since products of electron attachment will be slowly moving ions, the fast signal in a chamber is reduced.

Especially at low electrical fields the signal loss can be appreciable. For example, in the reaction with the most frequent impurity of oxygen

$$e^- + O_2 \rightarrow O_2^-$$

the rate at which the electrons disappear is given by

$$\frac{d}{dt}[e^-] = k[e^-]\,[O_2].$$

The square brackets indicate the concentration of the species. For oxygen the reaction rate constant is $k = 6 \times 10^{11}\ M^{-1}\ s^{-1}$, when the concentrations are given in molar units, i.e., 1 ppm of O_2 implies a lifetime of approximately 1 μs. Therefore, all parts of the chamber and the liquid itself have to be cleaned carefully.

3.1. Chamber and liquid cleaning

The chamber cleaning is done in two steps. First, a chemical wet process and then a physical, dry cleaning. In the chemical treatment all parts are cleaned in an ultrasonic alkaline bath with proper detergents followed by rinsing with desalinated water in three steps. The last bath has to have a water purity corresponding to an ohmic volume resistivity of nearly 18 Ω cm. This ecologically beneficial process turned out to be completely sufficient, and alternative treatments like cleaning in acetone or ethanol ultrasonic baths have been abandoned. Drying in a ventilated furnace and immediate assembly in a clean bench are the last steps. It turned out to be important to remove all dielectric microparticles from the detector surfaces by vacuum-cleaning in order to maintain a high dielectric strength.

Typically, a few monolayers of impurity, mostly moisture, are left on the surfaces. They are removed by ion bombardment in an argon glow discharge and intermittent pumping [9]. Due to the energetic impact of the ions, adsorbed molecules are desorbed from the surfaces and pumped away. Mainly H_2 and CO molecules have been detected. After 1 h of processing, less than 10^{-2} of a monolayer impurity are left and the chambers are ready to be filled. This has to be done within about 24 h. Otherwise, diffusion from the bulk material onto the surface continues and recharges it with compounds like CO and CO_2. The glow discharge is a fast and cheap cleaning method well suited to the task at issue.

The liquids arrive with a guaranteed impurity of less than 1 per thousand, as checked by analytical methods using gas chromatography. The liquids first have to be degassed to remove air, protective argon or any other gases which might be dissolved in the liquid. Then, they are treated in a purification system as sketched in Fig. 3. By heating and cooling the lower and the upper vessel the liquid is forced in vacuo through molecular sieves, where polar molecules of small diameters are removed first by sieves of the type A4 and A5 and then larger ones by the type 13X. In addition, TMS is passed through Oxisorb[3] to extract small traces of O_2. This procedure is not necessary for TMP, because the low vapour pressure allows more efficient degassing. The system is also equipped with 0.5 μm stainless steel filters at its inlet and at the outlets, which trap any dust particles that might be present in the

[3] Trade mark, a cobalt-nickel alloy for chemical oxygen absorption.

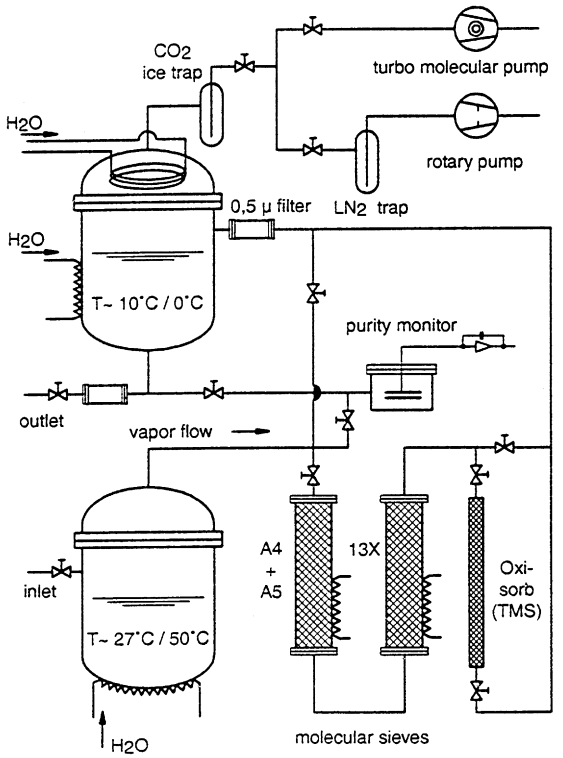

Fig. 3. Scheme of the purification system.

entering liquid or the purification lines. Finally, pumping is performed at regular intervals to remove any residual gas which escaped the initial degassing.

Using this system, about 50 l TMS or 25 l TMP are purified per day to a purity corresponding to an electron lifetime of about 30 μs. The lifetime is measured by diverting a small sample of purified liquid into a monitor cell. It consists of a parallel plate ionisation chamber with a ^{207}Bi source on the cathode and signal read-out on the anode. The signal height of the 1 MeV conversion electrons serves as purity indicator as described elsewhere [8].

Prior to the filling, the chambers are put into a vacuum box in order to evacuate them. Then, they are flushed with liquid which in turn is analysed in the monitor cell. If the chambers to be filled prove to be sufficiently clean, they are filled again and sealed off by cold welding of the Ni-filling nozzles. The chamber can then be operated for years with stable performance.

3.2. Electronics

3.2.1. Amplifier system

Due to the absence of internal charge amplification, liquid ionisation detectors exhibit a linear and stable signal behaviour. The feed-back amplifier chain is divided into a preamplifier mounted directly on the chamber to avoid parasitic capacitance of cable connections and a main amplifier located at the central electronics. A dynamic range of 1:50 000 is realised by a 13-bit digital read-out and a non-linear amplification characteristic for high pulses. This insures that the signal of one passing muon up to 10 GeV of deposited energy are read out without saturation.

Many authors have treated the problem of signal-to-noise optimisation in case of a high capacitive load [10–14] which in our case amounts to 600 pF. This made us design the front end amplifier as sketched in Fig. 4.

At the input, two JFET of the type 2SK371 with a high transductance of $g_s = 40$ mA/V and 75 pF input capacitance are connected in parallel to provide low serial noise. A collector current of 8 mA with 6 V voltage supply minimises the power dissipation without losing a good noise performance: 250 mW are consumed per circuit. They are carried off by water cooling of the preamplifier box which also contains the high-voltage distribution and decoupling capacitors. To ensure a sufficient heat conductivity, the electronic circuit board is embedded in quartz sand within the box.

The parallel noise is dominated by the gate current which corresponds to an equivalent noise resistor of 15 MΩ. To keep the noise low, the resistor of the feedback is set to 50 MΩ, and the high voltage is supplied to the anode by a 150 MΩ resistor. The coupling capacitor C_B is composed of three standard ceramic disk capacitors in parallel to attain 10 nF and to limit the corrections due to charge division to less than 6%. However, the capacitance also depends on the chamber voltage being reduced by about 20% at the maximum voltage of 6 kV. Correspondingly, corrections have to be taken into account.

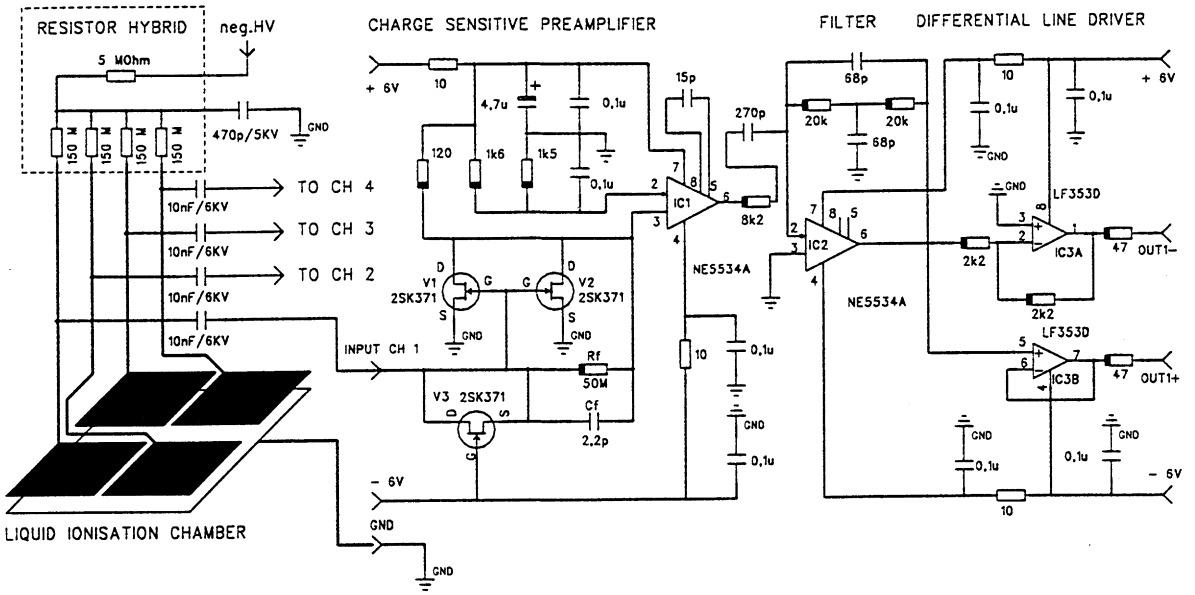

Fig. 4. Basic scheme of the preamplifier.

Via a precision capacitor of 12 pF ($\pm$ 1%), a test charge can be injected in order to calibrate the electronic chain. The applied voltage step rises within 250 ns. This is about the mean transit time of the ionisation electrons at the nominal voltage of 3 kV. To reduce the noise, a long shaping time of 8 μs has been chosen. As can be inferred from Fig. 4, on the preamplifier a $CR^2 = R^2C$ stage shapes to about 2 μs. Behind the active filter amplifier a differential output stage serves to drive symmetrically a 30 m long twisted pair cable connecting the preamplifier to the main amplifier.

On the main amplifier board the signal is received by a differential amplifier followed by three integration stages which shape the signal to 8 μs, as can be seen in Fig. 5. As a result, the noise has been brought down to an rms noise charge of 2100 e^- as the mean value for all 40 000 channels. This figure corresponds to a signal-to-noise factor for through-going muons of 1.8.

To cope with the large dynamic range, a nonlinear voltage characteristic has been adapted for energy depositions higher than 100 MeV. The nonlinearity is obtained by deliberately using saturation effects of the integration stages. The corresponding amplifier characteristic is measured by charge injection through the calibration capacitor. An example is shown in Fig. 6. The curve can be parametrized to better than 1% by a linear term in the lower charge region, an exponential form for mean values and a parabola in the upper charge region. The functions are matched to each other by means of the function tanh (ADC-k), tanh is used instead of a step function to ensure a steady transition at the point k. The parametrisation uses a 12-parameter formula which is reasonably fast to convert signals into energy. The calibration is repeated every six months, a stability within 2% for the first two years of running has been found.

3.2.2. *Digitization and read-out*

Both, the pre- and the main amplifier are realised as twin units on small hybrid boards. The latter are mounted on motherboards carrying 64 channels and are located in crates in the central counting-room. One crate contains 16 boards with a total of 1024 channels. Digitisation is performed by a sample- and- hold circuit which is integrated on the main amplifier board as well. A block diagram of the read-out electronics is shown in Fig. 7.

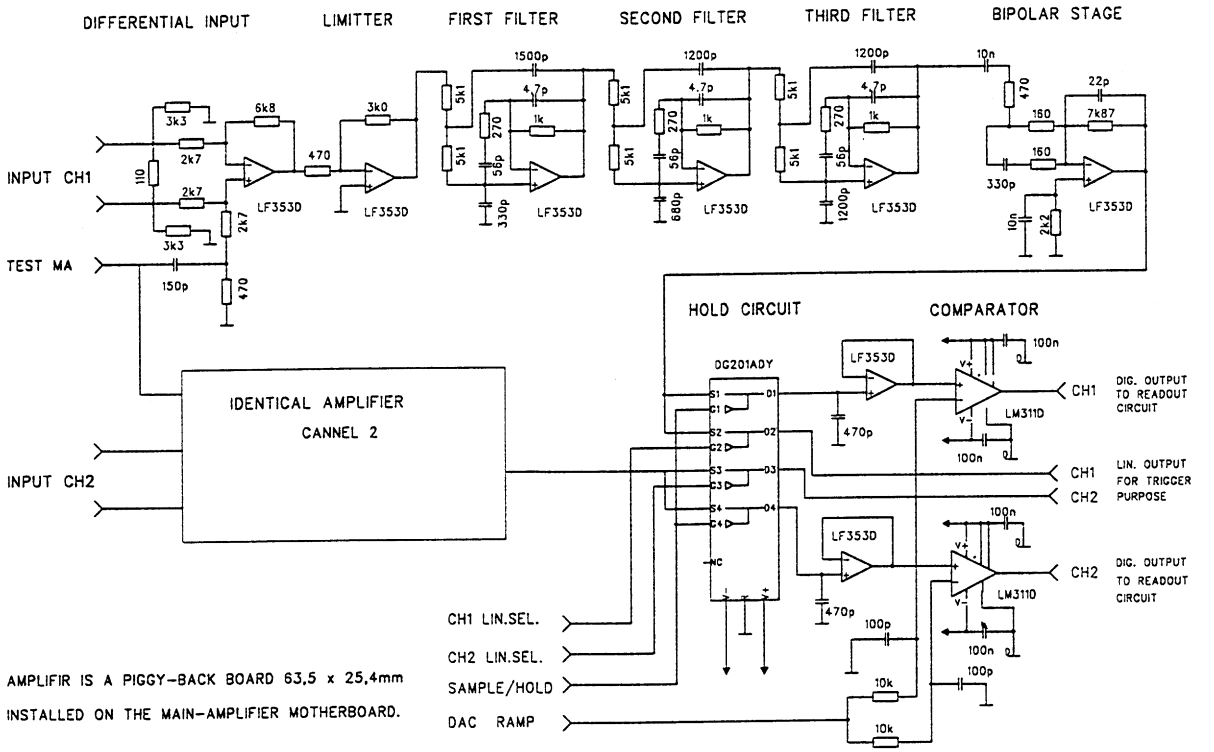

Fig. 5. Scheme of the main amplifier and sample- and-hold circuit.

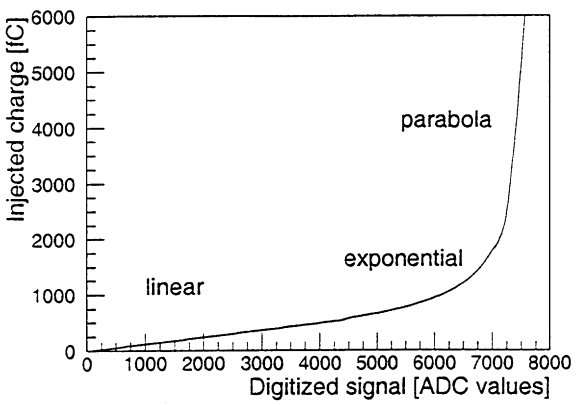

Fig. 6. Signal characteristic of the amplifier chain.

Eight MA-crates are combined and connected to a VME crate which is controlled by a transputer-based VME controller (TVC) [15]. Five of these units are installed in the experiment, each consisting of 8192 channels. When a trigger is generated, the sample- and- hold is switched to hold by the ADC control and a staircase reference voltage starts to rise being generated by the RMOD module. All 8192 channels in a VME crate are examined in parallel, and in total 40 960 channels are read out. At equal magnitude, a signal is sent to the ADC memory module which takes care of it. Ramping up the staircase voltage is terminated when all channels have replied. Thus, the conversion is stopped early if only small signals are present, and as a result dead time is reduced significantly. Maximum read-out time is 8 ms, typical values are about 3 ms. Further read-out of the digitized signals is managed in the VME crate by the TVC controller using an INMOS transputer T 805 as a processor. With the latter first data filtering like zero suppression is applied. Each individual channel has its proper threshold that corresponds to about 3σ, where σ is the rms value of the amplifier

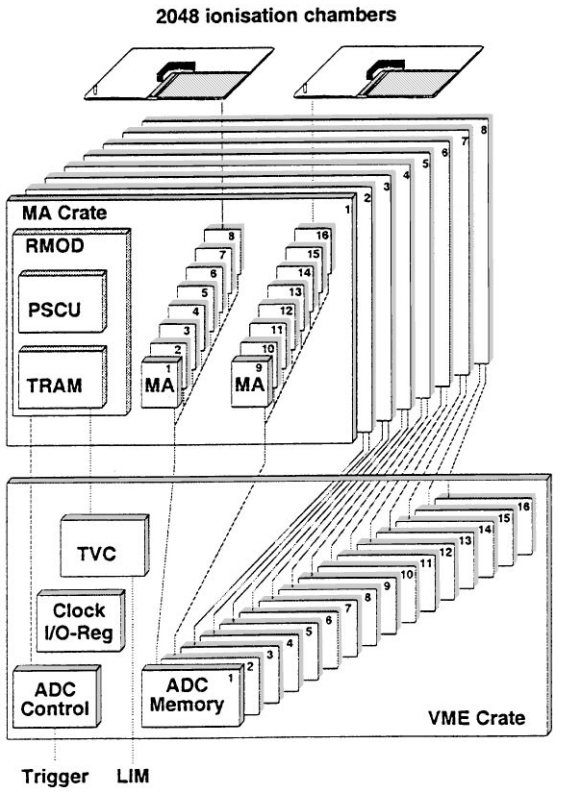

Fig. 7. Block diagram of the read-out electronics for 8192 channels.

noise. The data of all 5 VME crates are merged at the next level in the link interface module (LIM), before they are transmitted to a UNIX workstation.

3.3. Chamber test

After being filled and equipped with preamplifier boxes, the chambers are checked individually for their thickness and the liquid's purity. The thickness of the chamber is measured through the capacitance of each channel and obtained with an accuracy of 3%.

The electron lifetimes are determined by a two-days' check with cosmic-ray muons [16]. For this purpose, the chambers are put into a test stand as sketched in Fig. 8. Two layers of scintillators are arranged on top of each other and form two matrices to select muons. Between the upper and the lower matrix a Pb absorber ensures that only muons with an energy higher than 0.8 GeV are passing the set-up.

As an example of these tests, two plateau curves of the collected charge versus the applied voltage are shown in Fig. 9 for a typical chamber. In liquids the short thermalisation lengths of electrons ejected in the ionisation process entail a slight slope of the plateau, because at higher fields more and more electrons are prevented from recombining with their positive mother ions. In the example given, the electrons have a mean lifetime of 12 μs. The dashed curves indicate the maximum possible charge that could be collected in case of an infinite electron lifetime. The mean electron lifetime of all 6000 chambers filled with TMS as obtained from the tests is 9.5 μs. 200 chambers had to be rejected due to a lifetime of less than 1 μs. The reason in most cases were problems during pinch-off when air entered the chamber. These chambers have been emptied and refilled.

3.4. Signal stability

One of the principal motivations to use liquid ionisation chambers for a 10 yr cosmic-ray experiment is their long-term stability. The electronic feed-back amplifier chain fulfills this requirement. For the actual chamber signal, however, this remains to be proven. Individual chambers, therefore, have been tested repeatedly in a triton beam at the Karlsruhe [17,18] cyclotron, and with cosmic ray muons [16], where the signal of through-going particles has been monitored. Fig. 10 shows the collected charge of a particular chamber for several tests over a period of two years. No signal decrease is observed. On the contrary, a slight improvement might be noticed as has been reported amongst others by the Walic collaboration [19]. This signal increase can be attributed to the adhesion of a rest impurity present in the liquid onto the metal surfaces, which – if extremely clean – have a very polar character. In between the measurements, the chamber has been stored without an electric field applied.

The behaviour under a constant electric field strength can be deduced from the calorimeter

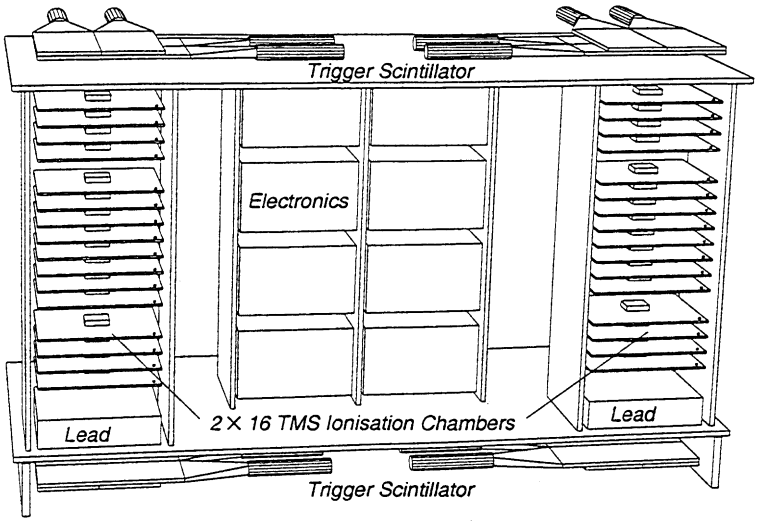

Fig. 8. Sketch of chamber test stand for check-out with cosmic-ray muons.

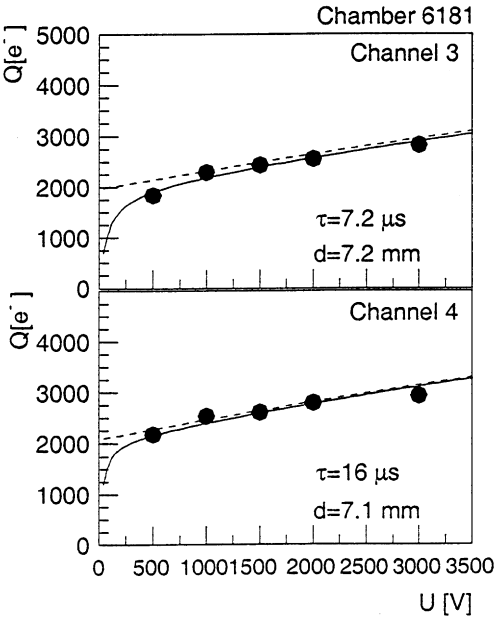

Fig. 9. Example of charge collected in an ionisation chamber during the course of a muon test run. The electron lifetime corresponds to a TMS impurity of 12 ppb oxygen equivalent.

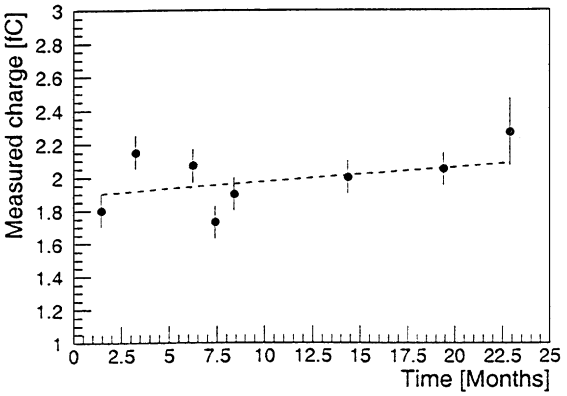

Fig. 10. Charge collected in a particular ionisation chamber at 2 kV for passing tritons of 96 MeV versus time of measurement.

performance and is documented in Fig. 11. It shows the average rate of single hadrons with an energy above the indicated threshold. As the flux of cosmic-ray hadrons and the energy spectrum are known to be very stable with time, the constant rate immediately reflects the signal stability of the chambers. Therefore, it may be concluded that impurity molecules neither diffuse from the bulk of the chamber material into the liquid nor does the liquid associate or dissociate under electrical stress. A very stable and reliable performance of the calorimeter can be ascertained for more than 3 yr from now, the first chambers being filled 6 years ago.

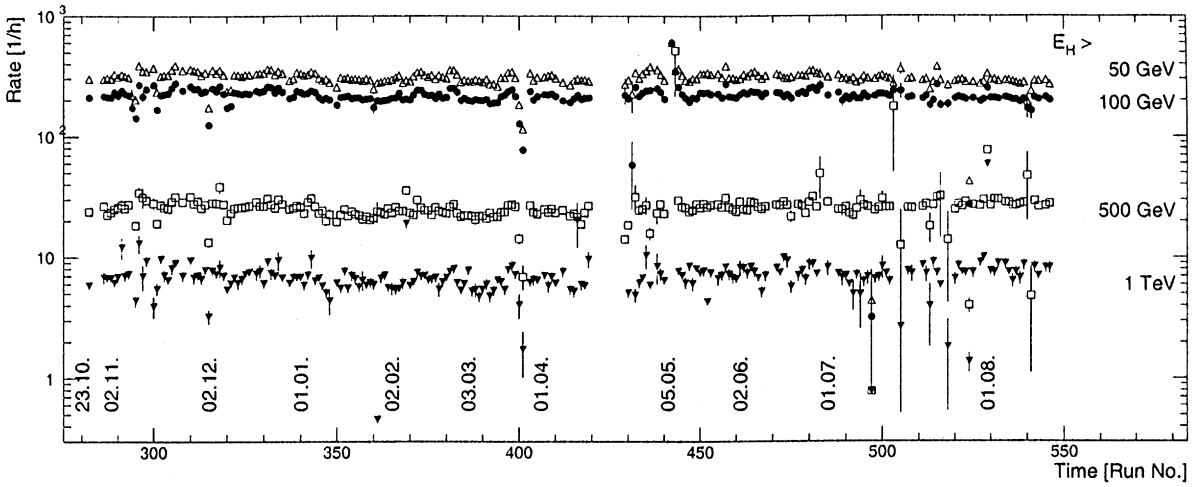

Fig. 11. Average hadron rate in the calorimeter per weekly time interval. The different symbols represent the indicated threshold energies.

4. Data selection and cascade reconstruction

4.1. Cascade reconstruction

To reconstruct the track and energy of hadrons in the calorimeter two algorithms have been set up. The first is trained to resolve in a shower core as many hadrons as possible and to reconstruct their proper energy and angle of incidence. The second is optimised to find single hadrons and to determine their energy and angle with best resolution. It is this latter algorithm which we are concerned with in the following.

The code has to meet different requirements. It has to accept angles of incidence of up to 60° and variable points of the first interaction. The angular resolution should be reasonably good to look for anisotropies in the arrival directions. Furthermore, the algorithm has to achieve a high efficiency for hadron recognition with a threshold as low as possible on the one hand and to obtain a high rejection power for other particles like electrons and muons on the other hand.

The program starts with a cluster algorithm analogous to a simple neural network. Channels with a relatively large energy deposition swallow stepwise the energy deposited in small buckets in adjacent cells. Thereby, electronic noise is suppressed and distinct energy clusters are obtained. These clusters can be displaced laterally from the local centre of energy deposition by up to the size of one pad. Subsequently, energy clusters in different planes are linked to form a trajectory. At least four clusters with more than 10 MeV energy, but not more than 80% of the energy in one cluster are required.

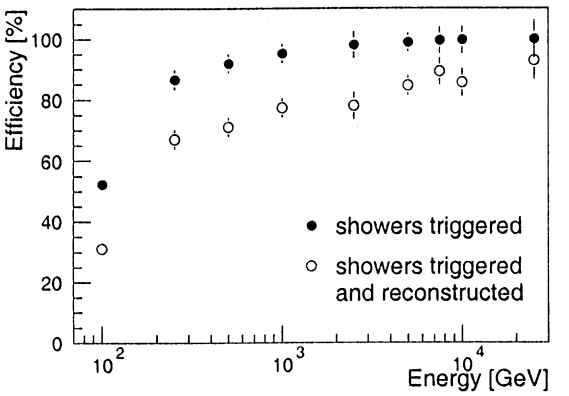

Fig. 12. Trigger efficiency (closed circles) and probability to trigger and reconstruct a hadron versus its energy (open circles).

The complete efficiency as calculated with the GEANT package [20] and using the FLUKA code

is given in Fig. 12. It shows the trigger efficiency and its combined efficiency with the shower recognition for particles of mean zenith angles of 18°. The trigger efficiency increases from 50% at 100 GeV to nearly 100% at around 2.5 TeV. At these high energies late converting hadrons evidently initiate large albedo effects. The shower recognition does not pass the 90% level even at the highest energies. This is due to the stringent requirement of energy clusters in the three upper layers to obtain a reasonably good angle determination. The angular resolution above 1 TeV reaches 2°. This precision will enable a sky survey with single hadrons in case of sufficient statistics being accumulated.

4.2. Energy estimation

To reconstruct the hadron energy from the measured charges, one needs to know the fraction of the hadron's energy that is deposited in the active medium. This fraction is usually obtained in a beam test with particles of known energy. For hadrons in the TeV range, however, no test beam is presently available. We have to rely on Monte Carlo simulations to evaluate this fraction at higher energies, extrapolating from lower energies where the simulations have been shown to reproduce the experimental results [21]. The simulations are performed with the GEANT code using FLUKA for the hadronic interactions. The energy is attributed according to the energies deposited in the second and the following layers. The first layer is omitted because at energies in the TeV region the accompanying electromagnetic radiation alters the calibration. The energy of an event is determined from a weighted sum, the weights being the absorber thickness in front of the active layer. Additionally, all detector effects such as side and rear leakage and electronic noise are taken into account as well as the chamber response to minimum ionising and densely ionising particles as published elsewhere [17,18]. As a result, the factor to convert the measured energy sum into energy of the infalling hadron turns out to be 250 at 100 GeV, but decreases slowly to 200 at 10 TeV.

5. Results

When attributing an energy to a hadron on the basis of its deposited energy, we cannot check whether the simulation predicts the correct incident energy or not. If the Monte Carlo program is wrong we might compare hadrons with simulations of a different energy. We can, however, check whether the simulation reproduces the pattern of energy deposition in the detector correctly and obtain confidence in the code. For this purpose, we compare the longitudinal and lateral distributions of showers of the same reconstructed energy.

5.1. Transition curves

The longitudinal development is shown in Fig. 13 and Fig. 14. In the former, the influence of trigger condition and shower recognition on the transition curves is demonstrated. Plotted are MC simulations employing FLUKA for infalling protons of 0.5 to 25 TeV energy. The curves represent fits of the data to the parametrisation $ct^a e^{-bt}$, t being the material in nuclear interaction lengths in front of each point. This ansatz has been derived for electromagnetic cascades but can be used – as we infer from the simulations – for hadronic showers in the same way.

It is observed that the trigger preferably selects showers with a high energy deposition in the front part, so does the shower pattern recognition program. This effect is particularly pronounced for the low-energy showers, where the above formula does not fit the actually measured data in the front part of the calorimeter. However, at the highest energies the experimental threshold is low enough to allow a trigger even for late converting particles by their albedo energy. At 25 TeV as net result, the measured curves resemble well the mean transition curves.

The experimental data obtained are shown in Fig. 14, presented in a manner similar to that of Fig. 13. At the higher energies, the simulations reproduce the experimental data quite well. In particular, no indication of a flattening of the exponential decay can be seen. Such a behaviour was claimed to have been detected with the Tien Shan calorimeter around 10 TeV and above by Yakovlev [22].

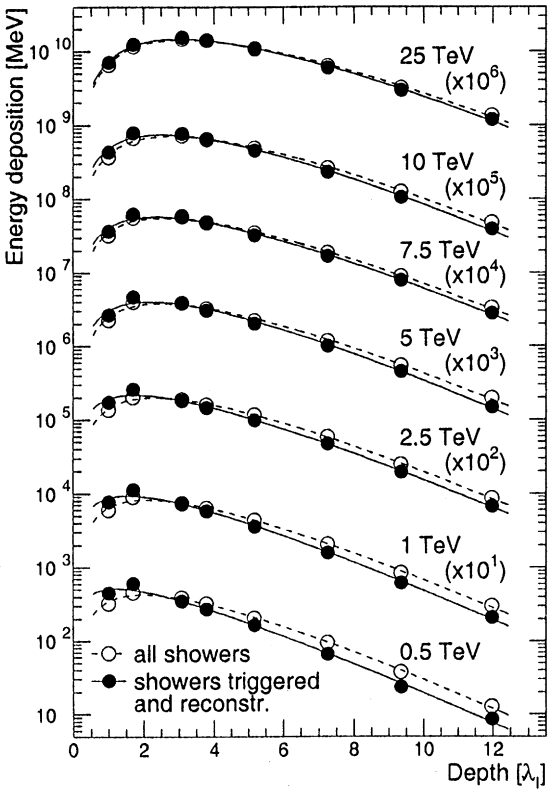

Fig. 13. Longitudinal transition curves obtained by MC simulations using the FLUKA code. Protons with 0.5–25 TeV energy. The energy depositions are multiplied by the indicated factors for a clear presentation. The curves represent fits of $ct^a e^{-bt}$ to the data points.

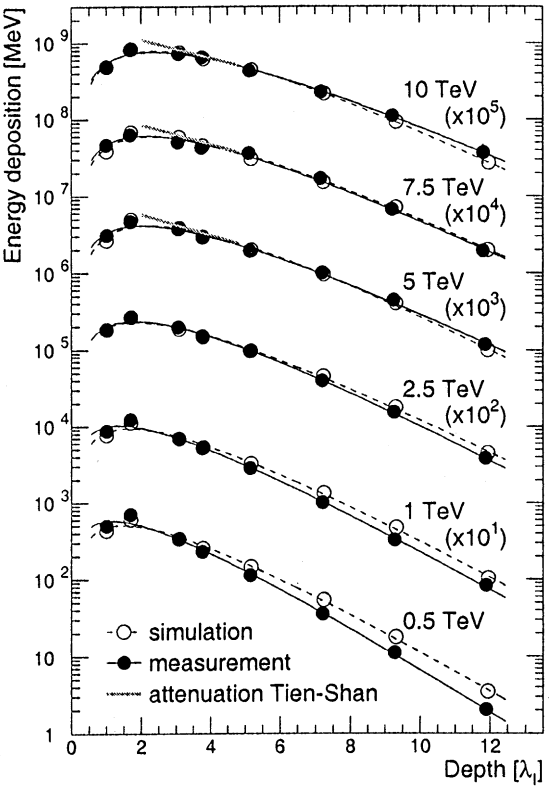

Fig. 14. Experimental transition curves (full circles) compared to simulated transition curves (open circles) using the FLUKA code.

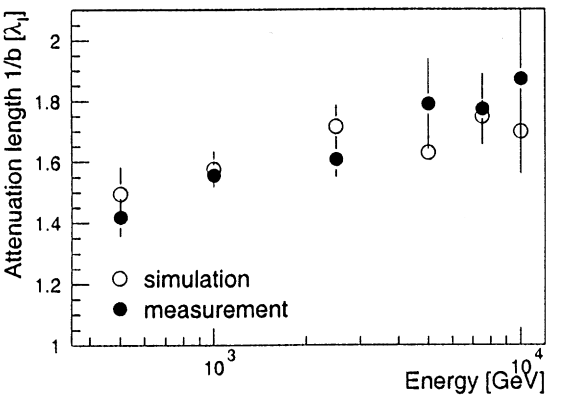

Fig. 15. Attenuation length in iron versus energy.

The slopes as detected with the Tien Shan lead calorimeter are indicated in the three upper transition curves. Their positions and lengths correspond to the Tien Shan calorimeter in interaction lengths. The slight increase with energy is well in accordance with the FLUKA simulations and mostly due to the logarithmic shift of the maximum deeper into the calorimeter. The attenuation lengths $1/b$ as obtained by fits to the experimental data are shown in Fig. 15 with respect to the energy and compared with FLUKA simulations. A slight increase is present in both. We do not observe a deviation from the simulation, at least not in the last three transition curves.

At lower energies the cascades seem to enter deeper into the absorber. However, this is probably an artifact caused by instrumental effects. At these energies the energy deposition in a chamber is low and still in the MeV region where the amplifier noise cannot be neglected. In the simulation it is

taken into account as a mean value with a Gaussian distribution. This may not be realistic enough to simulate the data correctly. Consequently, the slight differences should not be taken as major discrepancies.

5.2. Cascade fluctuations

Fluctuations are known to strongly influence the cascades of hadrons, at least much stronger than those of electromagnetic showers which develop in a more regular manner. We have measured hadron cascades of up to 50 TeV and at these high energies even hadron cascades contain an enormous number of particles. Hence, a smoother behaviour than at lower energies should be expected. This is not the case as demonstrated by Fig. 16, showing two particular cascades compared to the corresponding mean transition curves which represent 100 simulated cascades. In fact, the fluctuations depend to a lesser extent on the number than on the type of particles produced. A well-known example is the pion production, where the number of π^0 generated influences strongly to the further development of a cascade.

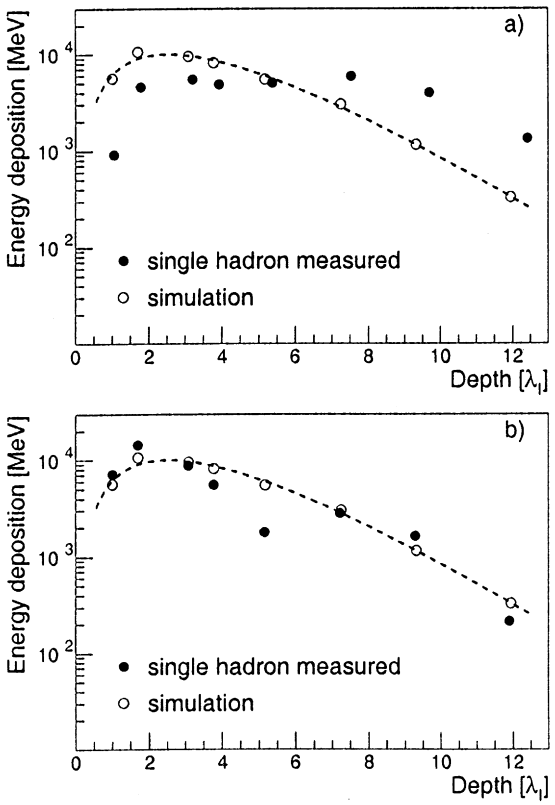

Fig. 16. Two examples of individual hadron cascades compared with the mean transition curves, both of 12 TeV.

5.3. Lateral energy deposition

A comparison of lateral energy distributions as obtained by measurements and simulations is shown in Fig. 17. Presented is the decrease of energy deposition of layers 4 and 6, which are situated deep enough not to be influenced by accompanying electromagnetic radiation created somewhere in the air above the detector. The experimental findings are well reproduced by the simulations in the cascade core up to a distance of about 35 cm. This is the radius of a cylinder around the shower axis where 90% of the hadron energy is found, and approximately corresponds to the effective absorption length of the calorimeter structure, calculated to be $\lambda_{\text{eff}} = 29$ cm.

The flattening in the very centre within 10 cm is an instrumental effect due to the finite pad size of 25 cm. The analogous data of the prototype calorimeter unfolded are shown in Fig. 18. They present the energy deposition in layer 3. It is obvious that, when unfolded, measured and simulated data exhibit in the centre an exponential fall-off. As for the large calorimeter, both agree with each other.

At larger distances the simulations reveal an exponential decrease less strong with a change in the slope at around 35 cm. Energy deposition in this halo region is conjectured to be caused by low-energy neutrons which penetrate easier to these outer regions than charged particles due to their low interaction cross-section. We have studied the effect by treating the neutrons in the simulations separately. It turned out that they are only partly responsible for the kink and low-energy electromagnetic particles make up the halo as well.

TMS and TMP with their large fraction of hydrogen are sensitive to the neutrons and efficiently detect the recoil protons. The corresponding efficiency of the chambers has been thoroughly studied at cyclotron energies [17,18]. In contrast to the

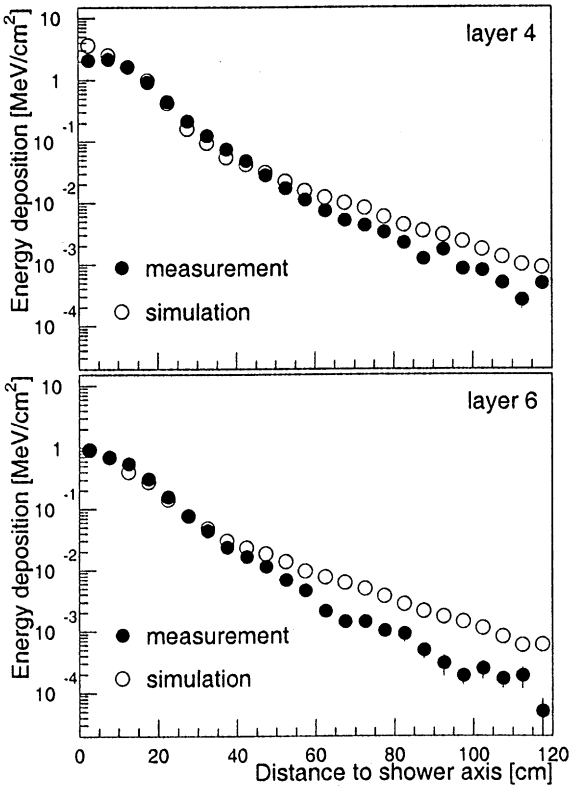

Fig. 17. Energy deposition with respect to the lateral displacement from the shower axis. Mean values for 5 TeV showers in the layers 4 and 6. Measurements (full circles) compared to FLUKA simulations (open circles).

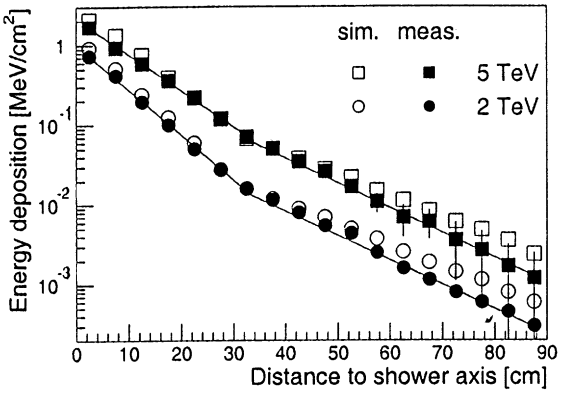

Fig. 18. Lateral energy deposition in the third layer as measured with the prototype. The experimental data are unfolded with respect to the finite pad size of $25 \times 25\ \mathrm{cm}^2$ acceptance.

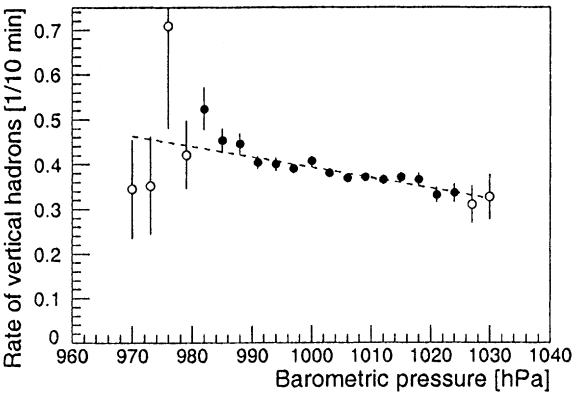

Fig. 19. Counting rate of hadrons with energy above 250 GeV in the calorimeter versus barometric pressure. The dashed line represents an exponential fit for which only the black points have been used.

simulations, the data indicate smaller amounts of deposited energy in the halo region. The flattening of the exponential decrease is much less or not pronounced at all. With the prototype calorimeter the effect has been observed in the same way as can be seen in Fig. 18. It is a small effect that does not influence the central energy determination. However, it is observed in all layers and at all energies. As a result, hadron cascades overlap less strongly and individual hadrons in dense jets of particles or in cosmic-ray shower cores can be separated more easily.

5.4. Nuclear attenuation length

The long-term stability of an ionisation chamber read-out allows to measure observables which otherwise are difficult to reveal like the anisotropy of cosmic radiation, which is a small effect in the order of 5×10^{-4}, or the inelasticity of nuclear interactions which needs large statistics. In order to determine the anisotropy or check whether the hadron flux is constant with time, the measured flux has to be corrected for atmospheric conditions.

Barometric pressure changes imply a change in the amount of air that has been traversed by the particles and influence the flux accordingly. For hadrons the barometric effect is relatively large. We have determined it for different energy intervals. As

an example, the flux variation for 250 GeV hadrons is shown in Fig. 19. It has a coefficient of 0.84%/hPa corresponding to an attenuation length of $\lambda_{att} = 121\ g/cm^2$, which is well in accordance with attenuation lengths obtained from flux measurements at different altitudes.

6. Summary and outlook

The large warm-liquid calorimeter of the KASCADE experiment has been operated for more than three years under stable and reliable conditions. With 6000 l TMP and 12000 l of TMS employed and 40 000 analog electronic channels of a large dynamic range of 1:50000 it is one of the largest calorimeter ever used. Single hadrons from 50 GeV up to 50 TeV have been detected. The average transition curves have been found to agree well with the longitudinal energy deposition simulated with the Monte Carlo program FLUKA as implemented in the GEANT code. The data on lateral development also agree with the simulations in the central region near the shower axis. However, less energy is found in the halo region outside a cylinder with a diameter of one effective interaction length.

The stable performance of the chambers allows to set forth a long scientific programme that will enable the study subtle questions in cosmic-ray research.

Acknowledgements

The authors would like to thank all members of the KASCADE collaboration for making the data used available. Special thanks go to many colleagues who helped to make the large calorimeter work successfully, in particular Daniela Boos, Heike Deris, Wolfgang Paulus, Michael Riegel, Doris Wochele, Peter Ziegler, and many others. Without their engagement and enthusiasm the enormous task of constructing the calorimeter would not have been accomplished.

References

[1] P. Doll et al., The Karlsruhe Cosmic Ray Project KASCADE, KfK 4686, Kernforschungszentrum Karlsruhe, 1990.
[2] H.O. Klages et al., Nucl. Phys. B (Proc. Suppl.) 52B (1997) 92.
[3] H.H. Mielke et al., Nucl. Instr. and Meth. A 360 (1995) 367.
[4] P.A. Aarmio et al., FLUKA user's guide. Technical Report, TIS-RP-190, CERN, 1987, 1990.
[5] FLUKA: Hadronic benchmarks and applications, Proceedings MC 93, International. Conference on Monte Carlo Simulation in High-Energy and Nuclear Physics, Tallahassee, Flo, 22–26 February 1993.
[6] M. Brendle, U. Raidt, Nucl. Instr. and Meth. A 412 (1998) 420.
[7] J. Engler, J. Phys. G. 22 (1996) 1.
[8] J. Engler, J. Knapp, G. Vater, Nucl. Instr. and Meth. A 327 (1993) 102.
[9] J. Engler, D. Moucka, J. Wochele, Nucl. Instr. and Meth. B 100 (1995) 183.
[10] W.J. Willis, V. Radeka, Nucl. Instr. and Meth. 120 (1974) 221.
[11] V. Radeka, IEEE Trans. Nucl. Sci. NS-21 (1974) 51.
[12] G. Gatti, P.F. Manfredi, D. Marioli, Nucl. Instr. Meth. 193 (1982) 539.
[13] C. Bacci et al., Nucl. Instr. and Meth. A 273 (1988) 321.
[14] C. Bacci et al., Nucl. Instr. and Meth A 279 (1989) 169.
[15] H. Leich, Transputer Based VME Controller, IfH DESY Zeuthen, 1991, unpublished.
[16] J. Hörandel, Kalibration von TMS-Ionisationskammern mit Myonen der Höhenstrahlung und Messung des Myonenflusses, KfK 5320, Kernforschungszentrum Karlsruhe, 1994.
[17] J. Engler et al., Nucl. Instr. and Meth. A 311 (1992) 479.
[18] J. Engler et al., Nucl. Instr. and Meth A 327 (1993) 128.
[19] B. Aubert et al, Walic Collaboration, Nucl. Instr. and Meth. A 316 (1992) 165.
[20] GEANT 3.15, Detector Description and Simulation Tool, CERN Program Library Long Writeup W5013, CERN, 1993.
[21] J. Engler et al., Nucl. Instr. and Meth. A 320 (1992) 460.
[22] V.F. Yakovlev, Proceedings of the seventh International Symposium on very High Energy Cosmic-ray Interactions, Ann Arbor, American Institute of Physics, 1992, p. 154, ISBN 1-56396-038-9.